Design Optimization of an Axial-Flux Reluctance Magnetic Coupling based on a Two-Dimensional Semi-Analytical Model

Thierry Lubin, Amir Abbas Vahaj, Akbar Rahideh

Design Optimization of an Axial-Flux Reluctance Magnetic Coupling based on a Two-Dimensional Semi-Analytical Model

Thierry LUBIN [1*], Amir Abbas VAHAJ [2], Akbar RAHIDEH[2]

[1] Groupe de Recherche en Energie Electrique de Nancy (GREEN), Faculté des Sciences et Technologies, Université de Lorraine, 54506 Vandœuvre-lès-Nancy, France.
[2]Department of Electrical and Electronics Engineering, Shiraz University of Technology, Shiraz 13876-71557, Iran
[*]Thierry.lubin@univ-lorraine.fr

Abstract: In this paper, design optimization of an axial flux reluctance magnetic coupling is presented. The optimal design procedure is based on a 2-D semi-analytical model defined at the mean radius combined with a multi-objective genetic algorithm (NSGA-II). In order to take into account the end-effects in the radial direction, a correction factor is defined to improve the torque and the axial force determination. The obtained results are compared with those of 3-D nonlinear finite element simulations and experimental results. It is shown that the proposed semi-analytical model is very accurate and requires very little computing time.

1. Introduction

Magnetic couplings can be used to transmit rotational movement between two shafts through a sealed wall in order to avoid any contact with the product to be treated for safety or hygienic reasons. The torque transmission between the two shafts is carried out without contact by the interaction between magnetic fields in the air-gap.

There are two main types of magnetic couplings: synchronous and asynchronous (eddy-current), with radial and axial flux topologies. The synchronous magnetic coupling [1, 2] consists of rare-earth permanent magnets (PMs) placed on both rotors that move at the same speed [3]. This kind of coupling has maximum transmittable torque, which is the highest value of torque that can be transmitted before the stall and called pull-out torque [4, 5]. For eddy-current magnetic couplings [6, 7], one of the two rotors consists of a conductive plate, which usually is copper. The torque transmission is due to the induced currents which depend on the relative speed between the two rotors (slip). This results in Joule losses [8, 9], and adequate cooling may be necessary to avoid overheating [10].

Among classical magnetic couplings technologies, reluctance torque magnetic couplings have received very little attention in the literature [11]. As shown in Fig. 1, an axial-flux reluctance magnetic coupling consists of two ferromagnetic discs facing each other and separated by a small air-gap. One side is equipped with sector-shaped rare-earth PMs magnetized in the axial direction with alternate polarity. The other side is made with mild steel salient poles with the same number as PMs. If one of the rotors is rotated, a change of stored energy will happen in the magnetic circuit. This change is resisted by a restoring torque toward the aligned position. The angular shift between the two discs is directly related to the transmitted torque value. In steady-state, the two rotors rotate at the same angular speed.

The main advantage of the reluctance magnetic couplings compared to more classical synchronous magnetic couplings with PMs on both sides is their durability in high-temperature environments, i.e. the side with salient-poles can be used in high-temperature environments and the other

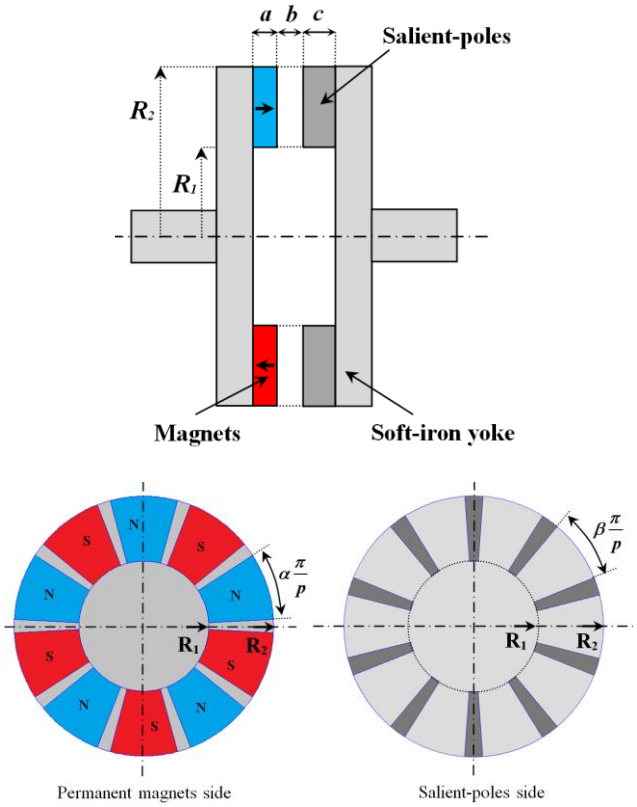

Fig. 1. *Cross section of the axial-flux reluctance magnetic coupling*

side with magnets can be used in room temperature. Besides, since fewer magnets have been used, the manufacturing price will reduce. On the other hand, the main drawback is lower torque density [11].

This paper is part of recently developed studies on the analytical modeling of magnetic couplings for their design [12-15]. Analytical models that can be found in the literature focus on more conventional topologies, such as those with permanent magnets on both sides [12, 13] or those with a copper disc on one side based on eddy currents

[14, 15]. For these structures where all the regions (magnet, air-gap, or copper) have the same geometry and therefore the same periodicity for the analytical solution, the analytical models are relatively simple. Here, the analytical model is more complicated due to the slotting effect (Fig. 2) which the operation of this magnetic coupling is based on it. Models already have been developed for the study of reluctance magnetic couplings but they are not suitable for use in an optimization procedure because they are too simple to predict the torque correctly [11] or they require too much computation time, i.e. 3-D finite element simulations [16].

In this paper, we propose a 2-D semi-analytical model based on the subdomains method (SDM). SDM is a semi-analytical method that consists of dividing the problem into the physical regions named subdomains. Then Maxwell's equations are solved analytically in each sub-domain [17-20]. This method gives accurate results when the slotting effect must be taken into account. This method has been applied for the study of permanent magnet machines [17, 18], PM linear motors considering different magnetization patterns [19] and study of the reluctance motors [20].

The semi-analytical model proposed in this paper is developed at the mean radius in Cartesian coordinate. A new correction factor is defined to take into account the 3-D effects in the radial direction. Then the model is used for multi-objective design optimization by helping the genetic algorithm. The results are compared with 3-D non-linear finite element simulations and experimental tests.

2. 2-D Semi-Analytical Model

To simplify the analytical modeling, we will consider a 2-D model defined at the mean radius R_m. As a result, the curvature effects and 3-D effects in the radial direction will be neglected. It has been shown that curvature effects can be neglected without great errors for axial-field actuators [13], [21]. On the other hand, the decay of the magnetic field on the radial edges of the magnetic coupling must be taken into account otherwise the pull-out torque and the axial force will overestimate. Hence, a correction factor will be introduced in the formula of the torque and axial force in order to take this effect into account.

2.1. 2-D Semi-analytical Model in the y-z

The 2-D model of the reluctance magnetic coupling at the mean radius is shown in Fig. 2. By considering this simplification, the cylindrical structure of Fig. 1 is made equivalent to a linear reluctance magnetic coupling. The model is then defined in a Cartesian coordinate system where the *y*-coordinate represents the circumferential direction and the *z*-coordinate the axial direction. An infinite dimension is considered in the *x*-direction. In addition, to obtain the simplest model, the following assumptions have been made:

- The iron parts (salient-pole and back-iron) have infinite magnetic permeability.
- The permanent magnets have a relative recoil permeability $\mu_r = 1$.

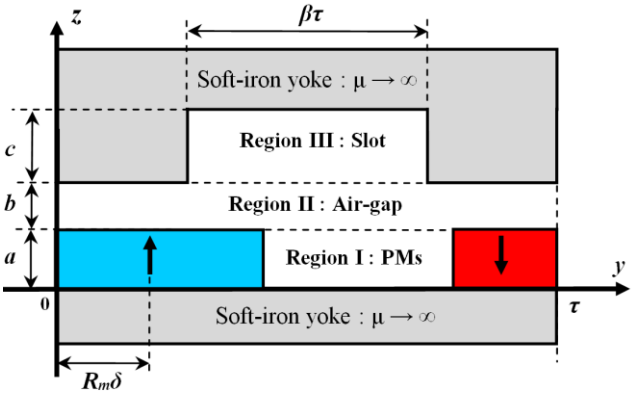

Fig. 2. *2-D model at the mean radius for one pole-pitch, y-z plane.*

The first hypothesis means that the magnetic saturation on the performance of the magnetic coupling has been neglected. This is the most important assumption and the principal limitation of the proposed model. However, in the next section, it will be shown that neglecting the magnetic saturation is not an issue, because the optimal shape of the salient poles corresponds to an unsaturated condition for the studied example. The second hypothesis implies using rare-earth permanent magnets (NdFeB or SmCo), but this is necessary to obtain good performances in terms of torque density [11].

As shown in Fig. 2, the entire domain is divided into 3 regions: Region *I* corresponds to the PMs, Region *II* is for the air-gap, and Region *III* shows the slot between two salient-pole. To compute the torque for different relative positions between the two rotors, the magnets (region I) can be shifted by an angle δ (torque angle) from the center of a salient-pole. As the problem presents a periodicity in the *y*-direction, the whole domain will be limited by $0 \le y \le \tau$, where τ is the pole-pitch. Also, because the whole domain is current-free, a magnetic scalar potential formulation is used to solve the problem. From the Maxwell equations, we obtain the following partial differential equation for each region ($i = I, II, III$).

$$\frac{\partial^2 \Phi_i}{\partial y^2} + \frac{\partial^2 \Phi_i}{\partial z^2} = 0 \quad \text{for} \quad i = I, II, III \tag{1}$$

where Φ_i is the magnetic scalar potential in region *i*. It is note worthy to say that the magnetization vector of the magnets presents only one independent component in the *z*-direction, hence the Laplace equation (1) is valid in the PMs region. According to the periodicity of the magnetic field distribution along the *y*-directions in the air-gap and PMs regions ($i = I, II$), solution of (1) is as follow:

$$\begin{aligned}\Phi_i(y,z) = &\sum_{k=1,3,5}^{K} \left(A^i e^{\alpha_k z} + B^i e^{-\alpha_k z}\right)\cos(\alpha_k y) \\ &+ \sum_{k=1,3,5}^{K} \left(C^i e^{\alpha_k z} + D^i e^{-\alpha_k z}\right)\sin(\alpha_k y)\end{aligned} \tag{2}$$

where A^i, B^i, C^i, and D^i are the integration constants which can be determined from the interface conditions between the regions, and $\alpha_k = k\pi/\tau$, k is a positive odd integer

The solution in the slot region is a bit more difficult to determine [20]. For this region, we have to consider the following boundary conditions:

$$\Phi_{III}\left(\frac{\tau}{2}(1-\beta),z\right)=0 \quad \text{and} \quad \Phi_{III}\left(\frac{\tau}{2}(1+\beta),z\right)=0 \tag{3}$$

Considering (1) and (3), the magnetic scalar potential in region III is as follows:

$$\Phi_{III}(y,z)=\sum_{n=1,2,3}^{N}\left(A^{III}e^{\lambda_n z}+B^{III}e^{-\lambda_n z}\right) \times\sin\left(\lambda_n\left(y-\frac{\tau}{2}(1+\beta)\right)\right) \tag{4}$$

where A^{III} and B^{III} are the integration constants in region III and $\lambda_n=n\pi/\beta\tau$, n is a positive integer.

As indicated previously, the 10 integration constants are obtained from the interface conditions between the regions, which lead to a linear system of 10 equations given in the appendix. The boundary conditions at $z = 0$ (region I) and $z = c$ (region III), and the interface condition between regions I and II at $z = b$ are easy to handle.

On the other hand, the interface condition between region II and region III at $z = b$ given by (5) is more difficult and corresponds to the main difficulty for this type of semi-analytical model. The method has been developed with great detail in [17]-[20] for cylindrical or rectangular problems and will therefore not be repeated here.

$$\Phi_{II}(y,b)=\begin{cases}\Phi_{III}(y,b) & \forall\, y\in\left[\frac{\tau}{2}(1-\beta),\frac{\tau}{2}(1+\beta)\right]\\ 0 & \text{elsewhere}\end{cases} \tag{5}$$

The next step is to determine the torque and axial-force expression from the Maxwell stress tensor. A line placed in the middle of the air-gap (region II) is taken as the integration path so the electromagnetic torque T_{2D} and the axial force F_{2D} can be expressed as follows:

$$T_{2D}=2p\frac{R_m H}{\mu_0}\int_0^{\tau}B_{yII}(y)B_{zII}(y)dy \tag{6}$$

$$F_{2D}=p\frac{H}{\mu_0}\int_0^{\tau}\left(B_{zII}^2(y)-B_{yII}^2(y)\right)dy \tag{7}$$

where B_{yII} and B_{zII} are the y- and z-component of the flux density in the air-gap which are derived from the magnetic scalar potential (2) as:

$$B_{yII}=-\mu_0\frac{\partial\Phi_{II}}{\partial y} \qquad B_{zII}=-\mu_0\frac{\partial\Phi_{II}}{\partial z} \tag{8}$$

where μ_0 is the vacuum permeability. Substituting (8) into (6) and (7), the analytical expressions for the electromagnetic torque and for the axial force become:

$$T_{2D}=\mu_0 2\pi p^2 H\sum_{k=1,3,5}^{K}k^2\left(A^{II}D^{II}-B^{II}C^{II}\right) \tag{9}$$

$$F_{2D}=\mu_0 2\pi p^2\frac{H}{R_m}\sum_{k=1,3,5}^{K}k^2\left(A^{II}B^{II}+C^{II}D^{II}\right) \tag{10}$$

At this point, it is worth noting that it is not possible to give a direct relation between the torque and the geometrical parameters, as it was the case for more simple magnetic couplings geometries without slotting effect [4, 10]. When the slotting effect is taken into account by using the sub-domain method [17]-[20], it is necessary to numerically invert a matrix to solve the system of 10 linear equations between the integration constants given in the appendix:

$$[M](X)=(S) \tag{11}$$

$$(X)=\left(A^I\ B^I\ C^I\ D^I\ A^{II}\ B^{II}\ C^{II}\ D^{II}\ A^{III}\ B^{III}\right)^t \tag{12}$$

where $[M]$ is the topological matrix, (X) is a vector of the integration constants which should be determined, and (S) is the source term which depends on the magnet distribution. A numerical solution of (11) can be obtained by using mathematical software (Matlab). Therefore, the proposed model is known as semi-analytical.

Because infinite dimension has been considered in the x-direction (radial direction), the torque and the axial force obtained from (9), (10) will have overestimation compared to the real value. This is due to the decay of the flux density on the radial edge of the magnets which is not taken into account in the torque and axial force expressions. To account for this 3-D effect, the following sub-section is dedicated to the definition of a correction factor.

2.2. Radial end effects, correction factor

In [4] that focused on axial flux magnetic coupling with PMs arranged on both discs, the radial dependence of the axial flux density in the air-gap has been measured. The results are recalled in Fig. 3. As it can be observed, the axial flux density drops down rapidly near the edges of the magnet whereas it was considered constant and equal to its value at the mean radius in the previous section, as shown by the thick line curve in Fig. 3. This assumption leads to an

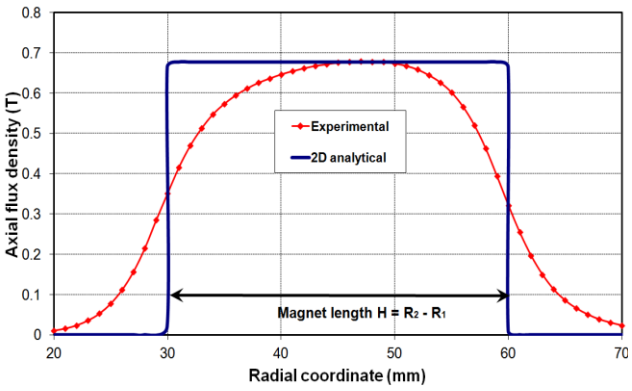

Fig. 3. *Radial dependence of the flux density in the air-gap [4].*

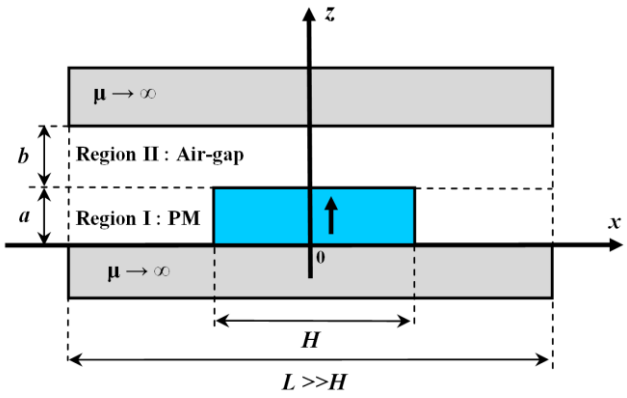

Fig. 4. *2-D model in the x-z plane at y = 0 (under a salient-pole)*

overestimation of the torque and the axial force [4].

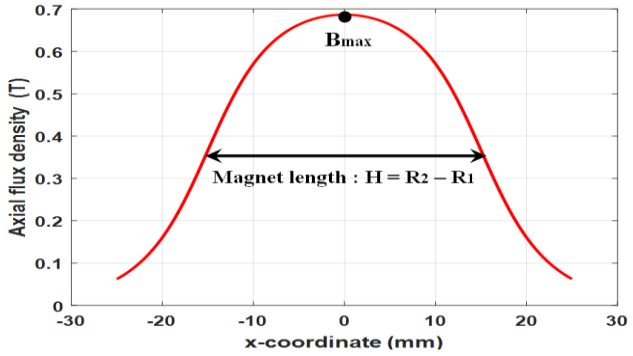

Fig. 5. *Axial flux density distribution along the x-direction*

In order to take into account this 3-D effect in a simple way and have a better estimation for the torque and the axial force, a correction factor K_e is introduced by carrying-out a supplementary 2-D analytical model in the *x-z* plane as shown in Fig. 4. The objective is to obtain the axial flux density distribution along the *x*-direction. We have to solve a problem with two regions having the same dimension, the correction factor is estimated under a salient-pole at $y = 0$. The domain is limited in the *x*-direction by imposing a perfect magnetic boundary condition at $x = \pm L/2$. In order to have no impact of this artificial boundary on the magnetic field determination, we impose $L>>H$. .

The axial component of the flux density defined at $z = a + b$ is given by:

$$B_{zII}(x) = \sum_{k=1,3,5}^{K} A_k \frac{\sinh\left(\frac{k\pi}{L}H\right)}{\sinh\left(\frac{k\pi}{L}(a+b)\right)} \cos\left(\frac{k\pi}{L}x\right) \qquad (13)$$

$$\text{with} \qquad A_k = \frac{4B_r}{k\pi}\cos\left(\frac{k\pi}{2L}H\right)$$

Fig. 5 shows the flux density distribution along the *x*-direction obtained from (13) with $H = 30$ mm, $a = 10$ mm and $b = 5$ mm. It can be observed that the waveform is close to the one obtained by measurement given in Fig. 3, but with a symmetrical aspect around $x = 0$.

Because the magnetic force varies with the square of the flux density, the correction factor K_e will be defined as:

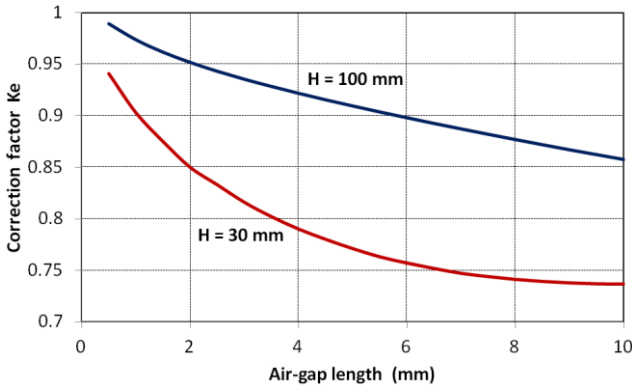

Fig. 6. *Impact of the air-gap length on the correction factor.*

$$K_e = \left(\frac{B_{avg}}{B_{\max}}\right)^2 \quad \text{with} \quad B_{avg} = \frac{1}{H}\int_{-H/2}^{H/2} B_{zII}(x)dx \qquad (14)$$

where B_{max} is defined at $x = 0$ as shown in Fig. 5.

Then the torque and axial force with the 3-D effects will be computed by combining (9) and (10) with (14) as:

$$T_{3D} = K_e T_{2D} \qquad \text{and} \qquad F_{3D} = K_e F_{2D} \qquad (15)$$

Variation of the correction factor as a function of air-gap length is given in Fig. 6 for $H = 30$ mm and $H = 100$ mm and considering a fixed value for the PMs thickness ($a = 10$ mm). These results show that the length of the air-gap and the radial length of the magnets have a significant impact on the value of the correction factor.

3. Comparison with 3-D Finite Element Simulation

In order to show the effectiveness of the proposed semi-analytical model, the results are compared with those obtained from 3-D finite-element simulations by considering the actual geometry of the reluctance magnetic coupling (Fig. 1). For the 3-D finite element simulations, we have used COMSOL Multiphysics® software with a scalar potential formulation (magnetostatic). The non-linear magnetic property (*B-H* curve) for the salient-pole has been considered in the FE analysis. The *B-H* characteristic is shown in Fig. 7.

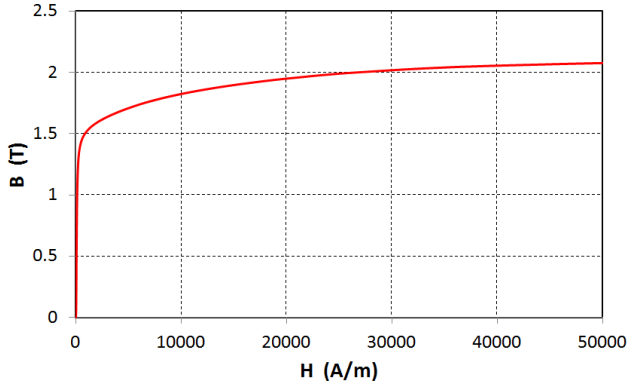

Fig. 7. *B-H curve for the iron parts (3-D FEM)*

Table 1: Geometrical parameters of the studied reluctance magnetic coupling

Symbol	Quantity	value
R_1	Inner radius of the magnets	30 mm
R_2	Outer radius of the magnets	60 mm
a	Magnets thickness	10 mm
b	Air-gap length	variable
c	Salient-pole thickness	15 mm
α	PMs pole-arc to pole-pitch ratio	0.83
β	Slot-opening to pole-pitch ratio	0.77
p	Pole-pairs number	5
B_r	Remanence of the magnets	1.25 T

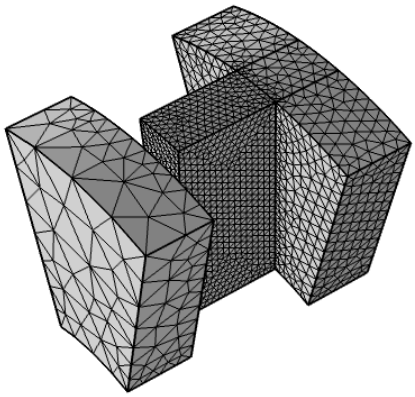

Fig. 8. *3-D FE simulations: mesh distribution in the magnet and in the iron parts.*

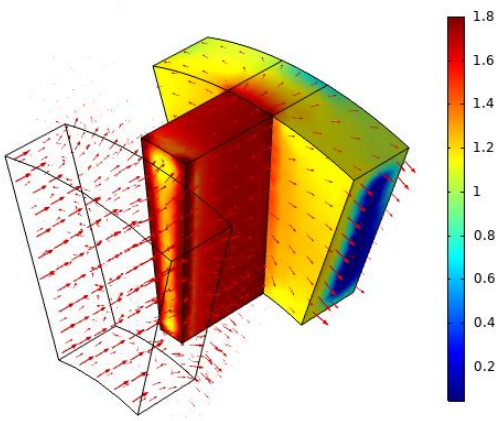

Fig. 9. *Flux line distribution under no-load condition obtained with 3-D FE simulation*

The mesh in the different regions has been refined until convergent results are obtained. The meshes in the magnet and in the iron part are shown in Fig. 8. Only 1 pole of the magnetic coupling has been considered in the FE analysis with anti-periodic boundary conditions in the circumferential direction. The air surrounding the magnetic coupling is considered in the FE simulation (an infinite box surround the system).

The geometrical parameters are given in Table 1. These values correspond to the ones obtained during an optimization procedure that will be presented in the next part.

The contours of magnetic flux density in the iron part under no load condition (δ = 0) obtained with the 3-D FE simulation is shown in Fig. 9. The flux density inside the teeth is around 1.4T, which is slightly below the knee point of the *B-H* curve shown in Fig. 7.

3.1. Flux Density Distribution in the Air-Gap

Fig. 10 shows the flux density distribution along the *y*-direction in the middle of the air-gap, at the mean radius, under no-load (δ = 0°) and full-load condition (δ = 9°). Due to the presence of the salient-pole, the flux density in the air gap has large variations, especially for the *y*-component. We can observe that very good agreements are obtained between the analytical results and the 3-D FE simulations

3.2. Pull-Out Torque

For a reluctance magnetic coupling [11], the torque is a function of sin(2$p\delta$), where δ is the torque angle, whereas it is a function of sin($p\delta$) for a magnetic coupling with PMs on the two discs [4]. This means that the pull-out torque T_{max} is reached for $\delta = \pi/4p$ that corresponds to δ = 9° for the studied coupling with p = 5.

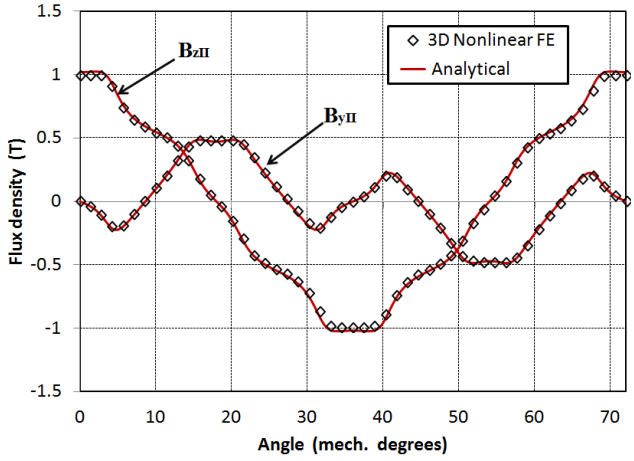

(a)

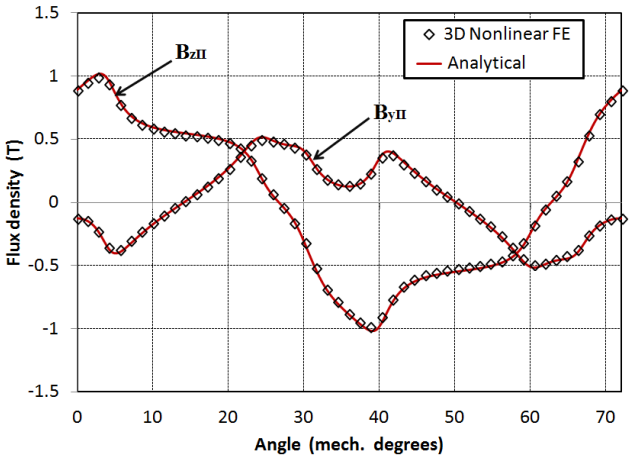

(b)

Fig. 10. *Flux density distribution along the y-direction in the middle of the air-gap for b = 3mm; (a) no load condition (δ = 0), (b) full load condition (δ = 9°).*

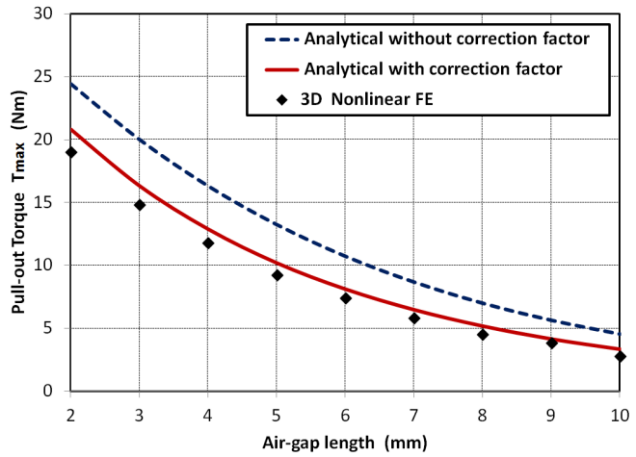

Fig. 11. *Pull-out torque versus the air-gap length with or without the correction factor.*

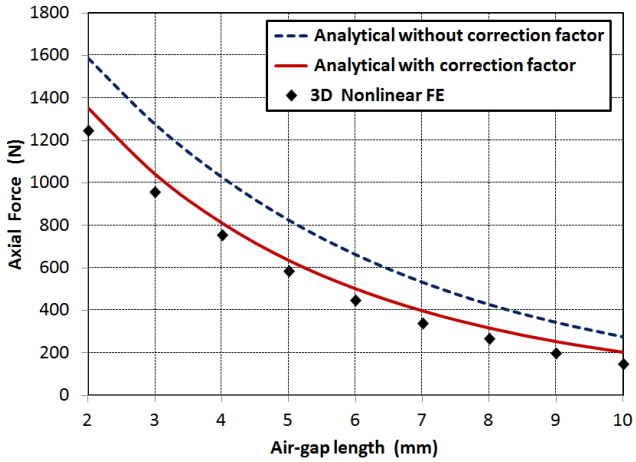

Fig. 12. *Axial force versus the air-gap length with or without correction factor.*

The air-gap length has a large influence on the performance of a magnetic coupling. Its value is imposed by the thickness of the sealing barrier between the two mechanical shafts. In order to show the effectiveness of the correction factor K_e on the torque prediction, Fig. 11 shows the pull-out torque as a function of air-gap length obtained without considering the correction factor (9) and taking it into account (15).

One can observe that the pull-out torque is well predicted by using the proposed semi-analytical model, even with changing the air-gap length. This result clearly shows the obtained gain in precision thanks to the correction factor. The error exceeds 30% without using the correction factor (9) and it is reduced to less than 10% when the correction factor is used (15). Another important result is a significant decrease in magnetic coupling performance as the air-gap increases. The pull-out torque goes from a value of 20 Nm for an air-gap of 2 mm to about 7 Nm for an air-gap of 6 mm, which corresponds to a decrease of around 65%.

3.3. Axial Force

The main disadvantage of an axial-flux magnetic coupling concerns the axial force between the two discs which affect the bearing losses of the drive [4]. It is therefore important to predict it accurately. The maximum value for the axial force corresponds to the no-load condition (i.e. δ = 0°). Fig. 12 shows the axial force as a function of the air-gap length with or without the correction factor. For the studied coupling, the axial force reaches a value of about 1000 N for an air-gap of 3 mm. Again, the correction factor greatly improves the predictions compared to 3-D nonlinear FE simulations.

3.4. Influence of Geometrical Parameters

In this section, the impact of some geometrical parameters on the performance of the magnetic coupling is studied. The main objective is to verify the correctness of the semi-analytical model in predicting the trend, compare to the 3-D non-linear FE results. The geometrical parameters are those given in Table 1. Only one parameter varies and other dimensions have been fixed.

It is well-known that the number of pole-pairs has a great impact on magnetic couplings performances. For a given air-gap length, there is always an optimum value. Fig. 13 shows that the analytical model is able to predict this optimal value which is equal to p = 4 for an air-gap b = 3 mm. In general, the optimal value for the number of pole-pairs decreases when the air-gap increases [4].

It can be seen in Fig. 13 that the torque prediction obtained with the semi-analytical model is underestimated for large number of pole-pairs and slightly overestimated for

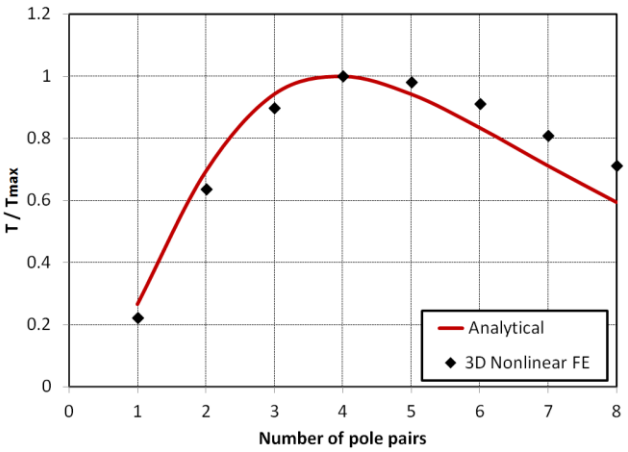

Fig. 13. *Torque versus the number of pole-pairs.*

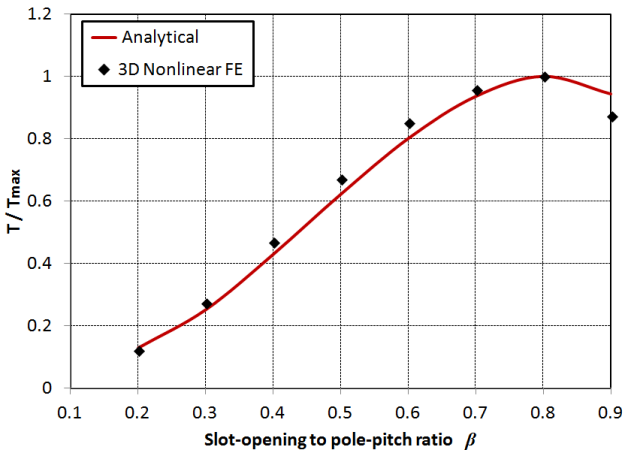

Fig. 14. *Torque versus the slot-opening to pole pitch ratio.*

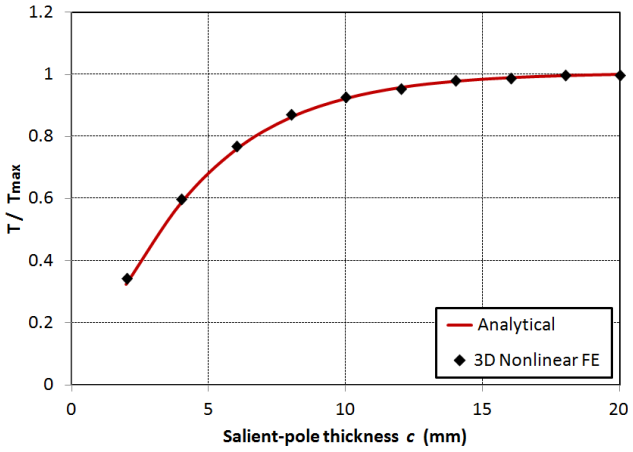

Fig. 15. *Torque versus the salient-pole thickness.*

p < 4. This is mainly due to the curvature effect that has been neglected in the proposed 2-D analytical model, while 3-D FE simulations take this effect into account [22].

For a reluctance magnetic coupling, another important parameter is the slot-opening to pole pitch ratio β as shown in Fig. 2. Fig. 14 shows that the maximum torque occurs for a large value of $\beta \approx 0.8$, which corresponds to a small opening angle for the salient-pole (20%) compared to the PMs pole-arc to pole pitch ratio (83%). This result is in agreement with a previously published paper about reluctance magnetic couplings [11]. When the salient-pole opening becomes very small (i.e. $\beta > 0.9$), magnetic saturation occurs and the torque decreases more rapidly than the one predicted by the semi-analytical model. This loss of accuracy for the analytical model will not be a problem for the optimization procedure because this area (very low value for the salient-pole opening angle) never corresponds to an optimal value.

Fig.15 depicts the torque versus the salient-pole thickness. It can be observed that the torque increases with the salient-pole thickness and becomes constant for $c \geq 15$ mm. This result indicates that it is important to choose this value carefully to obtain the best performance (not too small and not too big). Once again, very good prediction is obtained with the semi-analytical model.

4. Design optimization and experimental result

4.1. Design optimization procedure with GA

As the semi-analytical model is very fast in terms of computational time and very efficient in terms of precision, it will be used in a design optimization procedure. It is worth noting that 50 ms is needed to compute the torque with the analytical model whereas it takes over 40 s with 3-D FE simulations, which corresponds to a time saving of more than 800. It is well-known that Genetic Algorithm (GA) is a robust and effective tool in optimization problems. Here the multi-objective genetic algorithm NSGA-II, which is available in Matlab has been used. This algorithm will be coupled with the proposed semi-analytical model.

The flowchart for the optimization procedure is given in Fig. 16. Seven parameters (R_1/R_2, R_2, p, a, c, α, and β) need to optimize. Two objective functions that correspond to minimize the magnet volume (V_m) and the external radius (R_2) have been defined. Also, one constraint is imposed which corresponds to the desired pull-out torque (16 Nm) while the air-gap length is fixed to b = 3 mm. The optimization problem can be summarized as given in (16).

$$(P)\ \begin{cases} \min\limits_{x\in D} V_m(\boldsymbol{x}) \\ \min\limits_{x\in D} R_2 \\ \quad \text{with} \quad \boldsymbol{x} \in [R_1/R_2, R_2, p, a, c, \alpha, \beta] \\ \text{subject to : } \mathrm{T}(\boldsymbol{x}) \geq 16Nm \end{cases} \tag{16}$$

It should be noted that an additional constraint could be added in (16) to limit the maximum flux density in the salient-pole to avoid magnetic saturation effects ($B_{teeth} \leq$ 1.6T for example). Although the flux density in the salient-pole is not calculated with the proposed semi-analytical model (infinite permeability), it can be estimated from the z-component of the flux density in the air-gap (8) by applying the magnetic flux conservation. This issue has not been addressed in this paper.

The bounds of the variables in vector $\boldsymbol{x}$ (16) were chosen as follows: R_1/R_2 = 0.1-0.9; R_2 = 20-100 mm; p = 2-10; a = 2-20 mm; c = 2-25 mm; α = 0.1-0.9; β = 0.1-0.9. The optimization procedure uses 100 individuals evolving for 50 generations. It takes less than 30 s to obtain the Pareto front given in Fig. 17.

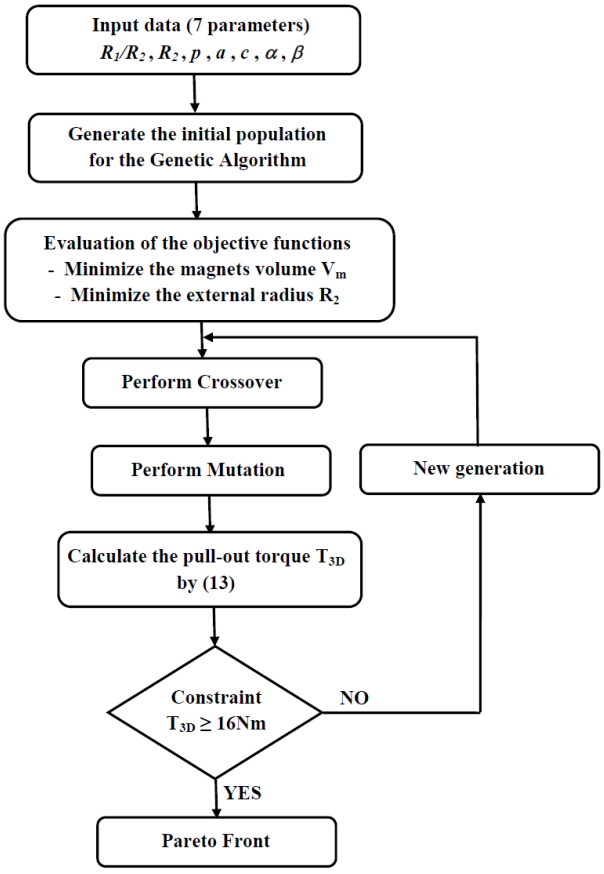

Fig. 16. *Flowchart of optimum design with GA*

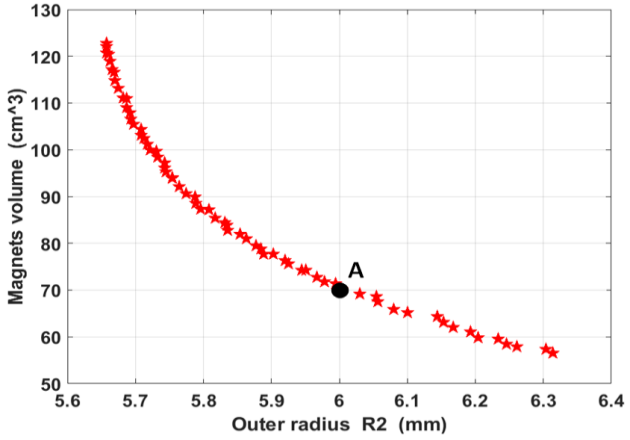

Fig. 17. *Pareto front obtained with GA: Magnets volume vs. Outer radius R_2 for T_{max} = 16 Nm.*

Table 2: Output optimal value for the design parameters obtained with GA

Symbol	Quantity	value
R_1/R_2	Outer radius/Inner radius	0.5
R_2	Outer radius of the magnets	60 mm
a	Magnets thickness	10 mm
c	Salient-pole thickness	15 mm
α	PMs pole-arc to pole-pitch ratio	0.83
β	Slot-opening to pole-pitch ratio	0.77
p	Pole-pairs number	5

It can be observed that the optimal value for the volume of the magnets and therefore the price of the magnetic coupling increases when the outer radius of the magnets decreases and vice versa. The solution noted A in Fig. 17 corresponds to the optimal parameters given in Table 2. These geometrical parameters are those corresponding to the prototype built for the experimental validations and presented in the following section.

4.2. Design optimization procedure with PSO

Particle Swarm Optimization (PSO) is a stochastic optimization method for non-linear functions. It is based on the reproduction of a social behavior. The origin of this method comes from observations made during computer simulations of flights in a group of birds and schools of fish [23]. These simulations highlighted the ability of individuals in a moving group to maintain an optimal distance from each other and to follow a global movement in relation to local movements in their neighborhood. This social behavior based on the analysis of the environment and the neighborhood is then a method of optimum search by observing the trends of neighboring individuals. Each individual tries to optimize his chances by following a tendency that he moderates by his own experiences. PSO has been largely used for the design optimization of electrical machines and actuators.

A multi-objective PSO technique is used for the design optimization of the studied magnetic coupling. The objective functions and the constraint are the same as the one defined in (16). The resulting Pareto front is given in Fig. 18. The obtained results from this method are close to those obtained with GA (Fig. 17). The magnets volume for

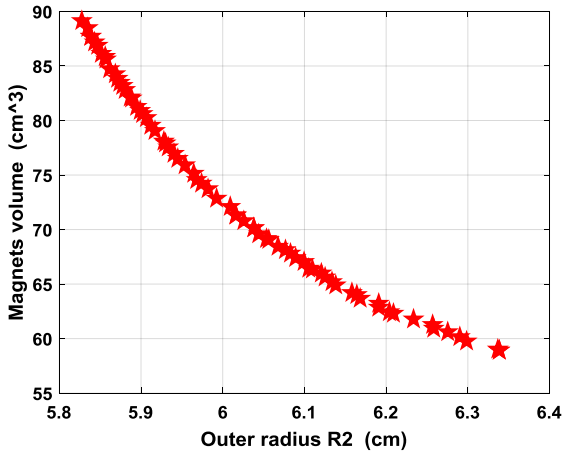

Fig. 18. *Pareto front obtained with PSO: Magnets volume vs. Outer radius R_2 for T_{max} = 16 Nm.*

an external radius R_2 = 6 cm is slightly higher (73 cm^3) than that obtained with the GA method (70 cm^3).

4.3. Static torque measurement

To validate the semi-analytical model from an experimental point of view and to check the performance of the magnetic coupling, we have manufactured the prototype shown in Fig. 19. Fig. 19(a) shows the salient-pole side

(a) *(b)*

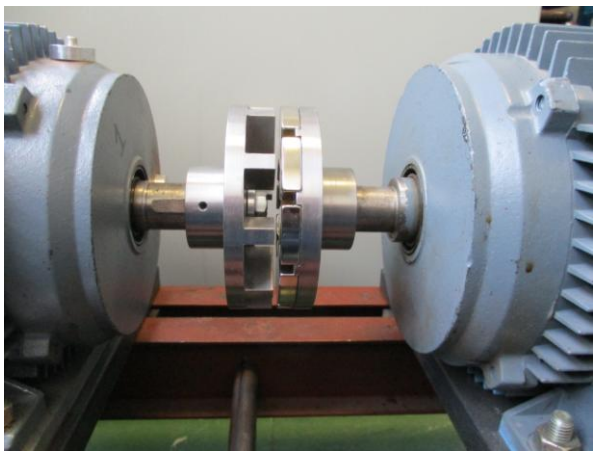

(c)

Fig. 19. *Reluctance magnetic coupling prototype. (a) salient-pole side, (b) PMs side, (c) Magnetic coupling placed between the two motors.*

which is composed of ten ferromagnetic teeth. The thickness of the back iron has been chosen to avoid magnetic saturation. We used low carbon steel (grade AISI-1010) with high relative permeability in the linear region of the *B-H* curve and a high level of saturation to improve the performance. The second disc is made using sector-type NdFeB glued on the iron yoke as shown in Fig. 19(b). The geometrical parameters are given in Table 1.

Fig. 20 shows the reluctance magnetic coupling placed on the test bench. The axial coupling is inserted between two electrical machines (DC motors, 3 kW, 1500 rpm). In fig. 20, the air-gap value is b = 3 mm. The air-gap length has been set by inserting non-magnetic plates of known thickness between the two discs. Figs. 20(a) and 20(b) respectively show a photograph and a block-scheme representation of the test bench arrangement for the static torque measurement. As shown in Fig. 20(b), the static torque was measured thanks to weights (250 g, 500 g, 1 kg) suspended to a rod (l = 1 m) locked to one rotor, the other being fixed. The relative angular position δ was measured using an incremental encoder with a resolution of 4096 pulses/revolution (precision of 0.088 degrees) and the data was transferred into a computer.

The measured static torque as a function of load angle δ is shown in Fig. 21 and is compared with the ones obtained with the semi-analytical model.

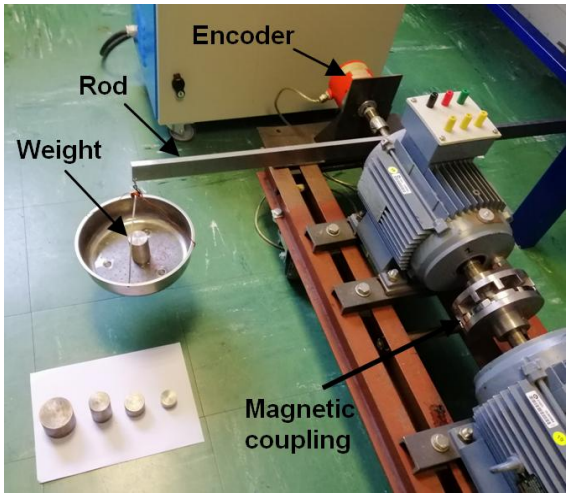

(a)

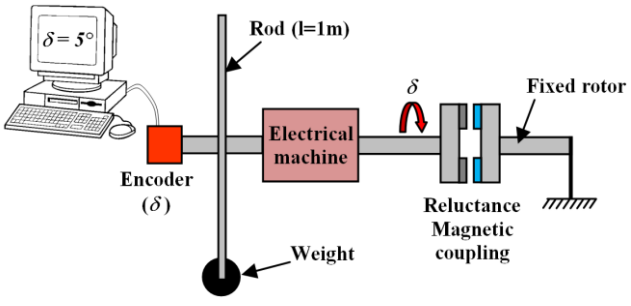

(b)

Fig. 20. *Experimental setup for the static torque measurement: (a) photograph, (b) block-scheme representation (top view).*

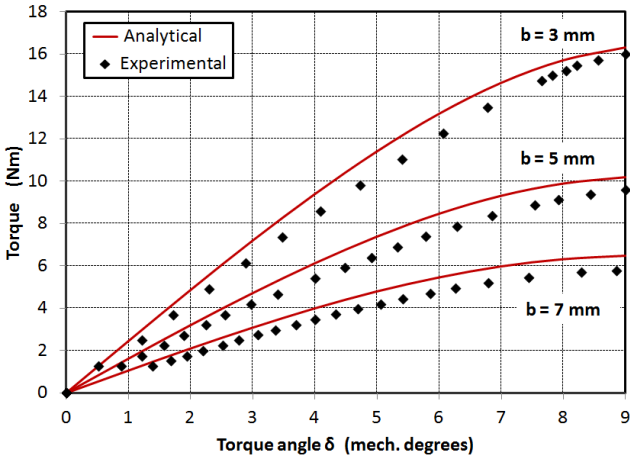

Fig. 21. *Measured and predicted static torque for three air-gap values.*

Three values for the air-gap were considered (b = 3 mm; 5 mm, and 7 mm). As shown in Fig. 21, good agreement between the measured and predicted torque values have been obtained, which clearly show the validity of the proposed analytical model. The error on the pull-out torque prediction is never greater than 10%. The small differences between the model and the tests can be explained by the test procedure to measure the load torque, which is relatively simple (weight suspended at the end of a long bar) and may lead to measurement errors.

5. Limitations of the semi-analytical model

In the proposed semi-analytical model, the curvature effect and the magnetic saturation of the iron parts have been neglected. Although we have obtained accurate results in sections 3 and 4 for the studied magnetic coupling, some lack of precision may occur for particular geometrical configurations of the magnetic coupling such as very low air-gap and tooth opening values (saturation effect), or for very low or very large values of the pole-pairs number where the curvature effect is more pronounced.

5.1. Curvature effect

As shown in [13] and [21], the curvature effects can be analyzed by considering a dimensionless number λ defines as the ratio of the radial excursion of the magnets H to the pole-pitch τ:

$$\lambda = \frac{H}{\tau} \quad \text{with} \quad H = R_2 - R_1 \quad \text{and} \quad \tau = \frac{\pi}{p} R_m \qquad (17)$$

A large value for λ means that the curvature is pronounced. In order to change the value of λ given in (15), the pole-pitch value is varied by changing the pole-pairs number from p = 1 to p = 10, which gives $0.42 < \lambda < 4.24$. The other geometrical parameters are kept constant and are those given in Table I with an air-gap value fixed to 3 mm.

Fig. 22 gives the relative error on the pull-out torque between the semi-analytical model and the 3-D FE simulations. It can be seen that the pull-out torque is predicted without error if the curvature coefficient $\lambda \simeq 1.8$. For lower or greater values of the curvature coefficient, the

relative error increases but remains below 10%, which is acceptable. This result confirms the ones obtained in [13] and [21] where it was shown that curvature effect can be neglected without great errors for axial-field actuators.

5.2. Magnetic saturation effect

As indicated previously, magnetic saturation is the most important assumption of the proposed model. Magnetic saturation occurs in the teeth and is highly dependent on the air-gap and tooth opening value, the smaller the air-gap or tooth opening, resulting in the greater the magnetic saturation effect.

In order to highlight the magnetic saturation effect on the pull-out torque, it has been computed for two values of the air-gap length (1 mm and 3 mm) and by varying the slot opening β, as shown in Fig. 23. Fig. 23 shows that magnetic saturation has a great impact on the pull-out torque for very low air-gap and tooth opening dimensions. It can be seen that the pull-out torque is well predicted until $\beta < 0.8$ for an air-gap of 3 mm whereas this value drops to $\beta < 0.7$ for an air-gap of 1 mm.

Fig. 23 shows that the optimal dimensions for the salient-pole correspond to the limit of the magnetic saturation (knee-point of the BH curve). It should be noted that an additional constraint could be added in the optimization procedure (Fig. 16) to limit the maximum flux density in the salient-pole to avoid magnetic saturation effects ($B_{teeth} \leqslant 1.6$T), then infinite permeability assumption will be valid.

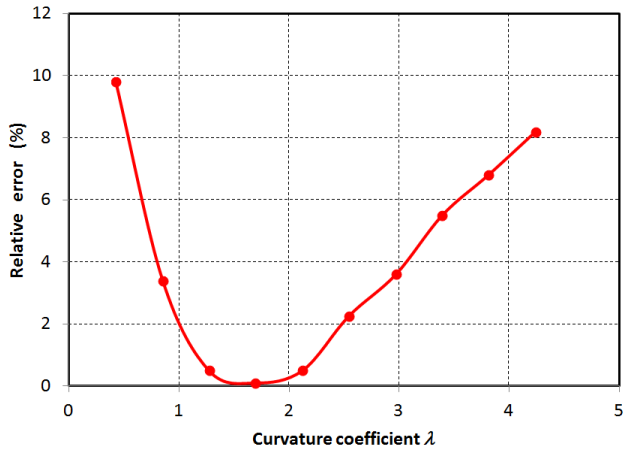

Fig. 22. *Curvature effect: relative error on the pull-out torque between 3-D FEM and the semi-analytical model.*

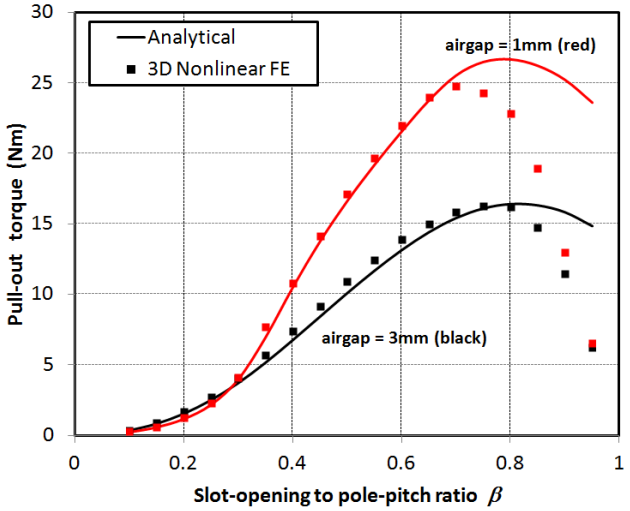

Fig. 23. *Magnetic saturation effect: pull-out torque versus the slot opening for two air-gap values: 1 mm and 3 mm.*

6. Conclusion

Reluctance magnetic coupling can be a solution for torque transmission between two shafts without contact. Compared to more classical synchronous magnetic couplings with permanent magnets on the two discs, it can be used in high temperature or corrosive environments. In this paper, we have developed a new analytical tool for the design optimization of a reluctance magnetic coupling. A correction factor has been proposed to take into account the 3-D effects in the radial direction. Comparisons with 3-D finite element simulations and measurements have shown the ability of the semi-analytical model in predicting the pull-out torque and the axial force with precision. Moreover, as the semi-analytical model is very effective in terms of computational time, it has been used in a design optimization procedure with multi-objective genetic algorithm. Finally, we have shown the limits of the model in terms of magnetic saturation.

7. References

[1] Hornreich R. M., Shtrikman S., "Optimal design of synchronous torque couplers," *IEEE Trans. Magn.*, 1978, **14**, (5), pp. 800–802.

[2] Charpentier J. F., Lemarquand G., "Optimal design of cylindrical air-gap synchronous permanent magnet couplings," *IEEE Trans. Magn.*, 1999, **35**, (2), pp. 1037–1046.

[3] Fontchastagner J., Lefèvre Y., Messine F., "Some co-axial magnetic couplings designed using an analytical model and an exact global optimization code," *IEEE Trans. Magn*., 2009, **45**, (3), pp. 1458–1461.

[4] Lubin T., Mezani S., Rezzoug A., "Simple analytical expressions for the force and torque of axial magnetic couplings," *IEEE Trans. Energy. Convers*., 2012, **27**, (2), pp. 536-546.

[5] Li K., Bird J. Z., Acharya V. M., "Ideal radial permanent magnet coupling torque density analysis," *IEEE Trans. Magn.*, 2017, **53**, (6), p. 8106304.

[6] Mohammadi S., Mirsalim M., 'Double-Sided permanent-magnet radial-flux eddy-current couplers: three-dimensional analytical modeling, static and transient study, and sensitivity analysis', *IET Electr. Power Appl.*, 2013, **7**, (9), pp. 665–679.

[7] Wang J., Zhu J., "A simple method for performance prediction of permanent magnet eddy current couplings using a new magnetic equivalent circuit model," *IEEE Trans. Ind. Electron.*, 2018, **65**, (3), pp. 2487-2495.

[8] Li Y., Lin H., Tao Q., Lu X., Yang H., Fang S., Fang H., "Analytical Analysis of an Adjustable-Speed Permanent Magnet Eddy-Current Coupling With a Non-Rotary Mechanical Flux Adjuster," *IEEE Trans. Magn.*, 2019, **55**, (6), p. 18670107.

[9] Aberoomand V., Mirsalim M., Fesharakifard A., "Design optimization of double-sided permanent-magnet axial eddy-current couplers for use in dynamic application," *IEEE Trans. Energy. Convers*., 2019, **34**, (2), pp. 909-920.

[10] Lubin T., Rezzoug A., "3-D analytical model for axial-flux eddy current couplings and brakes under steady-state conditions," *IEEE Trans. Magn.*, 2015, **51**, (10), p. 820371.

[11] Nagrial M. H., "Analysis and performance of variable reluctance (V. R.) torque coupler". *Proceedings IEEE Conference on Industrial Automation and Control Emerging Technology Applications*, 1995, pp. 136-139.

[12] Ravaud R., Lemarquand G., Lemarquand V., Depollier C., "Permanent magnet couplings: field and torque three-dimensional expressions based on the Coulombian model," *IEEE Trans. Magn*., 2009, **45**, (4), pp. 1950–1958.

[13] Dolisy B., Mezani S., Lubin T., Lévêque J., "A new analytical torque formula for axial field permanent magnets coupling," *IEEE Trans. Energy Convers.*, 2015, **30**, (3), pp. 892-899.

[14] Wang J., Lin H., Fang S., Huang Y., "A general analytical model of permanent magnet eddy current couplings," *IEEE Trans. Magn*., 2014, **50**, (1), p. 8000109.

[15] Dai X., Liang Q., Cao J., Long Y., Mo J., Wang S., "Analytical Modeling of Axial-Flux Permanent Magnet Eddy Current Couplings with a Slotted Conductor Topology," *IEEE Trans. Magn*., 2016, **52**, (2), p. 15720310.

[16] Wu W., H. Lovatt C., Dunlop J. C., "Analysis and design optimisation of magnetic couplings using 3D finite element modelling," *IEEE Trans. Magn.*, 1997, **33**, (5), pp. 4083–4085.

[17] Dubas F., Espanet C., "Analytical solution of the magnetic field in permanent-magnet motors taking into account slotting effect: no-load vector potential and flux density calculation," *IEEE Trans. Magn*., 2009, **45**, (5), pp. 2097-2109.

[18] Zhu Z. Q., Wu L. J. , Xia Z.P., "An accurate subdomain model for magnetic field computation in slotted surface-mounted permanent magnet machines," *IEEE Trans. Magn.*, 2010, **46**, (4), pp. 1100-1115.

[19] Rahideh A., Ghaffari A., Barzegar A., Mahmoudi A., "Analytical model of slotless brushless PM linear motors considering different magnetization patterns," *IEEE Trans. Energy Convers*., 2018, **33**, (4), pp. 1797-1804.

[20] Lubin T., Mezani S., Rezzoug A., "Exact analytical method for magnetic field computation in the air-gap of cylindrical electrical machines considering slotting effects," *IEEE Trans. Magn*., 2010, **46**, (4), pp. 1092-1099.

[21] De la Barrière O., Hlioui S., Ben-Ahmed H., Gabsi M., LoBue M., "3-D formal resolution of Maxwell equations for the computation of the no-load flux in an axial flux permanent-magnet synchronous machine," *IEEE Trans. Magn*., 2012, **48**, (1), pp. 128–136.

[22] Lubin T., Rezzoug A., "Improved 3-D analytical model for axial-flux eddy-current couplings with curvature effects," *IEEE Trans. Magn.*, 2017, **53**, (9), p. 17121736.

[23] Kennedy J., Eberhart R., "Particle swarm optimization," *IEEE Proc. Conf. on Neural Networks*, 1995, (4), pp. 1942–1948.

8. Nomenclature

R_1	Inner radius of the magnets.
R_2	Outer radius of the magnets.
R_m	Mean radius of the magnets ($R_m = (R_1+R_2)/2$).
H	Radial length of the magnets ($H = R_2 - R_1$).
a	Magnets thickness.
b	Air-gap length.
c	Salient-poles thickness.
α	Permanent magnets pole-arc to pole-pitch ratio
β	Slot-opening to pole-pitch ratio
p	Pole-pairs number.
B_r	Remanence of the magnets.
τ	Pole pitch ($\tau = R_m\pi/p$).

9. Appendix

The 10 integration constants are obtained by solving a linear system of 10 equations by using Matlab:

$$A^I + B^I = 0$$

$$C^I + D^I = 0$$

$$A^I e^{\alpha_k a} - B^I e^{-\alpha_k a} = A^{II} e^{\alpha_k a} - B^{II} e^{-\alpha_k a} - \frac{R_m K_k}{kp}\cos(kp\delta)$$

$$C^I e^{\alpha_k a} - D^I e^{-\alpha_k a} = C^{II} e^{\alpha_k a} - D^{II} e^{-\alpha_k a} - \frac{R_m K_k}{kp}\sin(kp\delta)$$

$$A^{II} e^{\alpha_k a} + B^{II} e^{-\alpha_k a} = A^I e^{\alpha_k a} + B^I e^{-\alpha_k z_1}$$

$$C^{II} e^{\alpha_k a} + D^{II} e^{-\alpha_k a} = C^I e^{\alpha_k a} + D^I e^{-\alpha_k z_1}$$

$$A^{II} e^{\alpha_k b} + B^{II} e^{-\alpha_k b} = \sum_{n=1}^{\infty} \frac{2p}{\pi}\left(A^{III} e^{\lambda_n b} + B^{III} e^{-\lambda_n b}\right) \times f(n,k)$$

$$C^{II} e^{\alpha_k b} + D^{II} e^{-\alpha_k b} = \sum_{n=1}^{\infty} \frac{2p}{\pi}\left(A^{III} e^{\lambda_n b} + B^{III} e^{-\lambda_n b}\right) \times g(n,k)$$

$$A^{III}e^{\lambda_n c} + B^{III}e^{-\lambda_n c} = 0$$

$$A^{III}e^{\lambda_n b} - B^{III}e^{-\lambda_n b} = \sum_{k=1}^{\infty}\frac{2kp}{n\pi}\left(A^{II}e^{\alpha_k b} - B^{II}e^{-\alpha_k b}\right)\times f\left(n,k\right) + \sum_{k=1}^{\infty}\frac{2kp}{n\pi}\left(C^{II}e^{\alpha_k b} - D^{II}e^{-\alpha_k b}\right)\times g\left(n,k\right) \quad \text{(A.1)}$$

with

$$f(n,k) = \int_{\frac{\tau}{2}(1-\beta)}^{\frac{\tau}{2}(1+\beta)} \cos(\alpha_k y)\sin\left(\lambda_n(y - \frac{\tau}{2}(1+\beta))\right)dy \quad \text{(A.2)}$$

$$g(n,k) = \int_{\frac{\tau}{2}(1-\beta)}^{\frac{\tau}{2}(1+\beta)} \sin(\alpha_k y)\sin\left(\lambda_n(y - \frac{\tau}{2}(1+\beta))\right)dy \quad \text{(A.3)}$$

$$K_k = \frac{4B_r}{\mu_o k\pi}\sin\left(k\alpha\frac{\pi}{2}\right) \quad \text{(A.4)}$$